

Movie S1. Deterministic-single-encapsulation of micro-beads

Movie S2. Deterministic-multi-encapsulation of micro-beads

Figure S1. (A-F) Lateral position distributions of each microbead at different flow rates. The concentration of microbeads was fixed to $8 \times 10^6 \text{ mL}^{-1}$ at all flow rates ($n = 300$ for each microbead).

Figure S2. (A) Schematic of our double-spiral chip. Fluidic resistance channels are segmented and labeled as numbers 1–4. (B) Electric circuit analogy of double-spiral chip.

Figure S3. Analysis of droplet-generation regime with respect to fluidic resistance channel. (A) Droplet generation without fluidic resistance channel. (B) Droplet generation with fluidic resistance channel. The light-blue region indicates an enlarged flow rate range, facilitating the generation of monodispersed droplets through the designed fluidic resistance channel; here, a represents the slope ($Q_o \propto 2Q_w^{-1}$).

Figure S4. Multi-fluorescence confocal microscopic images of five different combinations of clusters. The scale bars represent $10 \mu\text{m}$.

Figure S5. Volcano plots summarizing the differentially expressed gene (DEG) analysis of neutrophil clusters, cancer-cell clusters, and cancer-cell–neutrophil clusters generated from the double-spiral chip. (A) Volcano plot showing DEGs in the MCF-7-cell (low-metastatic breast cancer cell line) cluster compared to the HL-60-cell cluster, indicating 465 down-regulated genes (green) and 1744 up-regulated genes (red). (B) Volcano plot showing the DEGs of the paired MCF-7-cell and HL-60-cell clusters, indicating 368 up-regulated genes (red) with respect to the MCF-7-cell cluster. (C) Volcano plot showing the DEGs of the MDA-MB-231-cell (high-metastatic breast cancer cell line) cluster compared with the HL-60-cell clusters, indicating 215 down-regulated genes (green) and 1981 up-regulated genes (red). (D) Volcano plot showing the DEGs of the paired MCF-7-cell and HL-60-cell clusters, indicating 276 up-regulated genes (red) with respect to the MDA-MB-231-cell cluster.

Figure S6. Protein–protein interaction (PPI) network analysis of differentially expressed genes from (A) the clusters of MCF-7 cells with HL-60 cells and from (B) the clusters of MDA-MB-231 cells with HL-60 cells. The expression levels of (C) CCL24, (D) CCL4, (E) CCL22, (F) PPBP, and (G) CD69 were quantified by quantitative reverse transcription polymerase chain reaction (RT-qPCR) and exhibit significant over-expression in the clusters of both cancer cells and the HL-60 cells.

Table S1. Dimensionless numbers in the spiral channel with respect to flow rates

Table S2. Functions of the key transcripts

Electronic Supporting Information (ESI)

Microfluidic recapitulation of circulating tumor cell–neutrophil clusters via double spiral channel-induced deterministic encapsulation

Junhyun Park^a, Sunyoung Park^a, Kyung A. Hyun^{a,*} and Hyo-Il Jung ^{a,*}

^aDepartment of Mechanical Engineering, Yonsei University, Seoul, 03722, Republic of Korea.

*E-mail: hyunkkuplus@gmail.com, uridle7@yonsei.ac.kr

* Author to whom correspondence should be addressed: *E-mail: uridle7@yonsei.ac.kr (H.I.Jung); hyunkkuplus@gmail.com (K.A.Hyun)

2.3. Design of the microfluidic chip

To perform inertial focusing upon a particle in a microfluidic channel, the particle must undergo sufficient inertial lift forces at certain distances along the fluidic flow. To this end, the spiral channel for inertial focusing was designed with a long length; however, it exerted a high-pressure drop through the channel according to the Hagen–Poiseuille equation. Because droplet generation is strongly determined by the pressure or flow rate of each phase¹, the pressure drop of each phase must be balanced to generate monodispersed droplets. Hence, we designed a microfluidic channel using the Hagen–Poiseuille equation and an electric circuit analogy, to achieve both inertial focusing of the particle and the generation of monodispersed droplets.

The Hagen–Poiseuille equation expresses the pressure drop in the cylindrical channel and can also be applied in a microfluidic channel with a rectangular cross-section. The pressure drop [Pa] through the channel is expressed as

$$\Delta P = QR, \quad (4)$$

where Q is the volumetric flow rate [$\text{m}^3 \text{s}^{-1}$] and R is the hydraulic resistance of the fluidic channel [Pa s m^{-3}], defined as

$$R = \frac{12\eta L}{Wh^3(1 - 0.627\frac{h}{W})}, \quad (5)$$

where η is the dynamic viscosity of the fluid [Pa s], and L [m], W [m], and h [m] are the length, width, and height of the channel, respectively.

To match the pressure drop of each phase, we segmented each channel and labeled the fluidic resistance numbers as follows (Fig. S2A): R_1 denotes the fluidic resistance from the oil-phase injection to the split part of the oil phase; R_2 denotes the fluidic resistance from the split part of the oil phase to the droplet-generation junction; R_3 denotes the fluidic resistance of the spiral

channel, which is the water phase; and R_4 represents the fluidic resistance from the droplet-generation junction to the outlet. Because R_4 is an immiscible fluid flow (i.e., the droplet phase), it cannot be calculated using Eq. (5). Therefore, it was calculated considering only the flow of the oil phase. The actual fluidic resistance is higher than the assumed value because the droplet is a form of resistance in the channel.

Based on the segmented fluidic resistance, we analyzed the microfluidic chip via an electric circuit analogy (Fig. S2B). Because the electric current can be understood as a type of fluidic flow, physical similarities pertain between microfluidic channels and electric circuits². The volumetric flow rate corresponds to the electric current, the pressure drop through the channel corresponds to the electric voltage between two different nodes, and the hydraulic resistance corresponds to the electric resistance. Thus, Eq. (4) corresponds with Ohm's law, and the pressure drop of each phase can be expressed as

$$\Delta P_O = Q_O \times (R_1 + (R_2 \parallel R_2)), \quad (6)$$

where ΔP_O is the pressure drop from the oil-phase injection to the droplet-generation junction, and Q_O is the volumetric flow rate of the oil phase;

$$\Delta P_W = Q_W \times R_3, \quad (7)$$

where ΔP_W is the pressure drop in the spiral channel, and Q_W is the volumetric flow rate of the water phase; and

$$\Delta P_D = Q_O \times R_4, \quad (8)$$

where ΔP_D is the pressure drop from the droplet-generation junction to the outlet.

Assuming the flow rate ratios of the water-phase Q_W and oil-phase Q_O to be identical, we adjusted the magnitude of the fluidic resistances R_1 , R_2 , and R_4 by varying the length of the channel, to match the pressure drop of each phase.

To sum up the design of the microfluidic channel for the monodisperse droplet generation, the pressure drop between the water phase and oil phase should be balanced. In the case of the water-in-oil droplet, it was shown that the higher pressure exerted on the water phase than the oil phase resulted in no droplet formation³. To solve this phenomenon, the formation of the monodisperse droplet can be obtained by increasing the pressure exerted on the oil phase, which can be achieved by adjusting the hydraulic resistance of the fluidic channel. Accordingly, the formation of the monodisperse droplets can be achieved at high flow rates (generally, Weber number of the dispersed phase less than 1) by adjusting the dimensions of the microfluidic channels (i. e. length, width, and height).

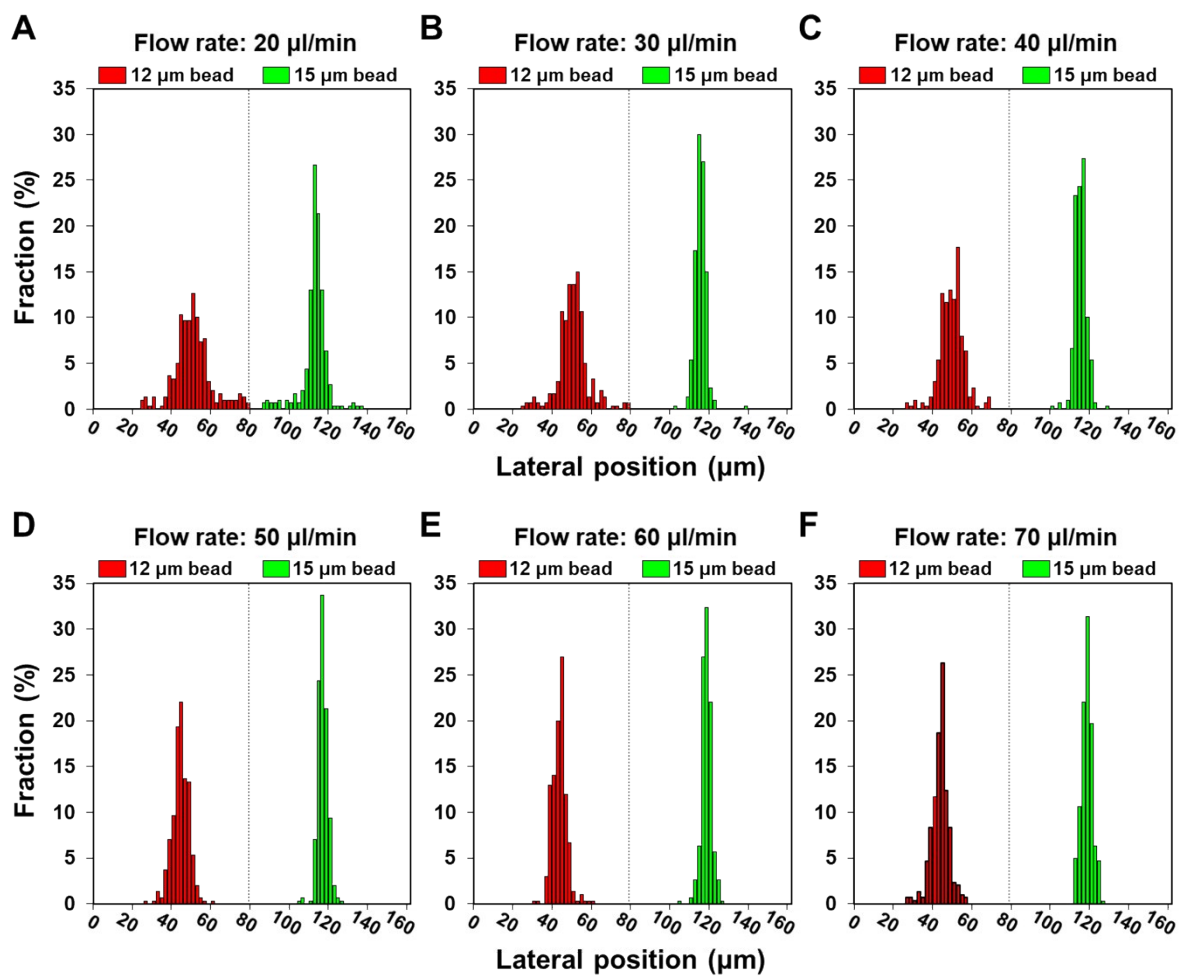


Fig. S1. (A-F) Lateral position distributions of each microbead at different flow rates. The concentration of microbeads was fixed to $8 \times 10^6 \text{ mL}^{-1}$ at all flow rates ($n = 300$ for each microbead).

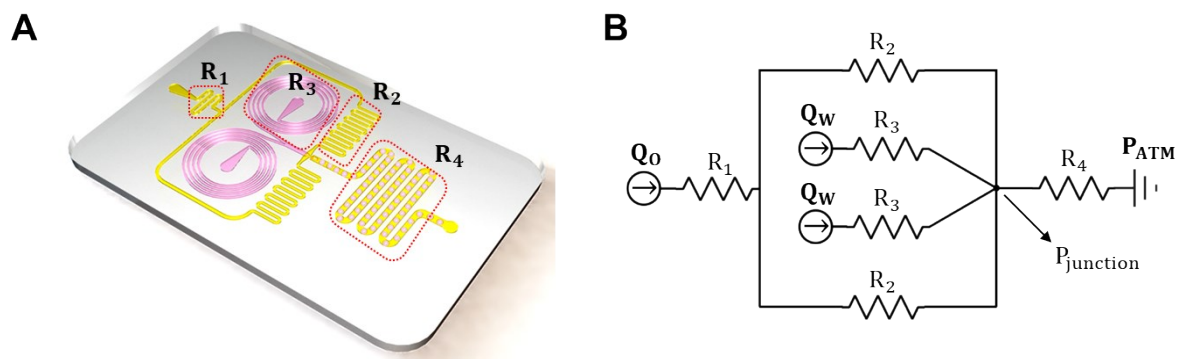


Fig. S2. (A) Schematic of our double-spiral chip. Fluidic resistance channels are segmented and labeled as numbers 1–4. (B) Electric circuit analogy of double-spiral chip.

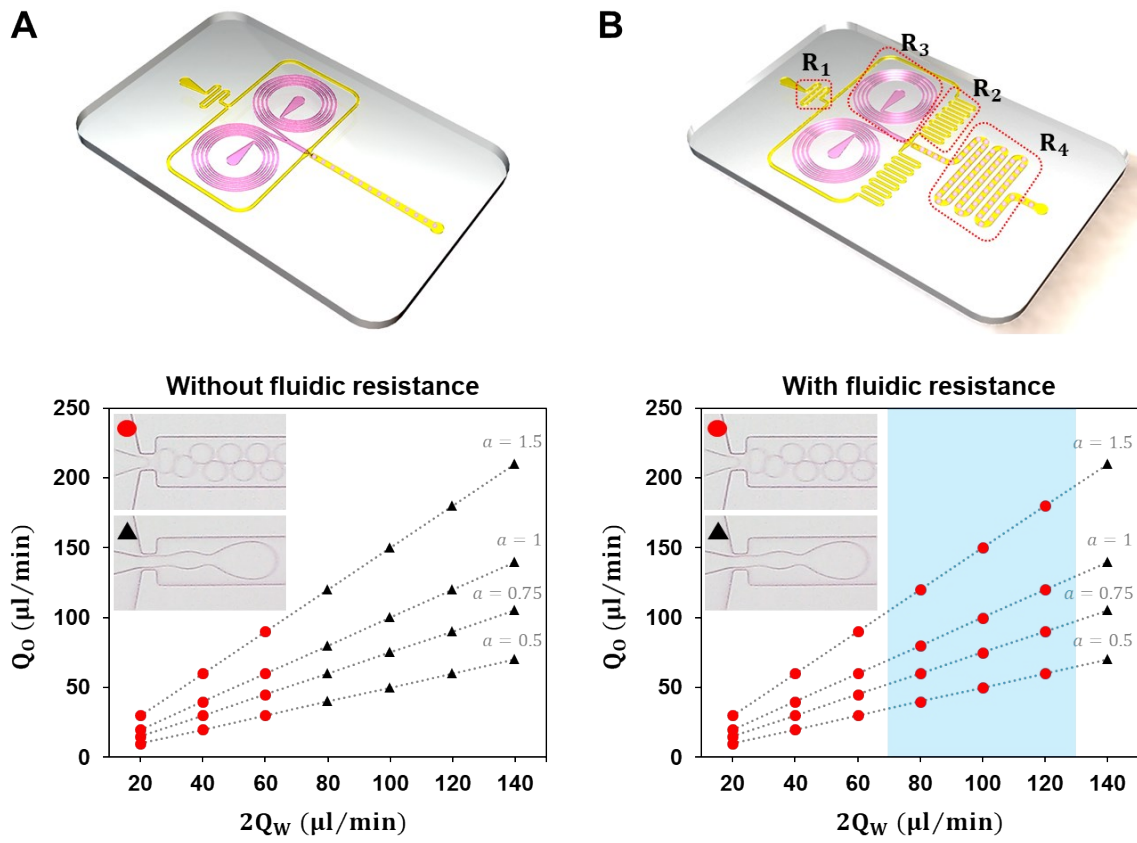


Fig. S3. Analysis of droplet-generation regime with respect to fluidic resistance channel. (A) Droplet generation without fluidic resistance channel. (B) Droplet generation with fluidic resistance channel. The light-blue region indicates an enlarged flow rate range, facilitating the generation of monodispersed droplets through the designed fluidic resistance channel; here, a represents the slope ($Q_O 2Q_W^{-1}$).

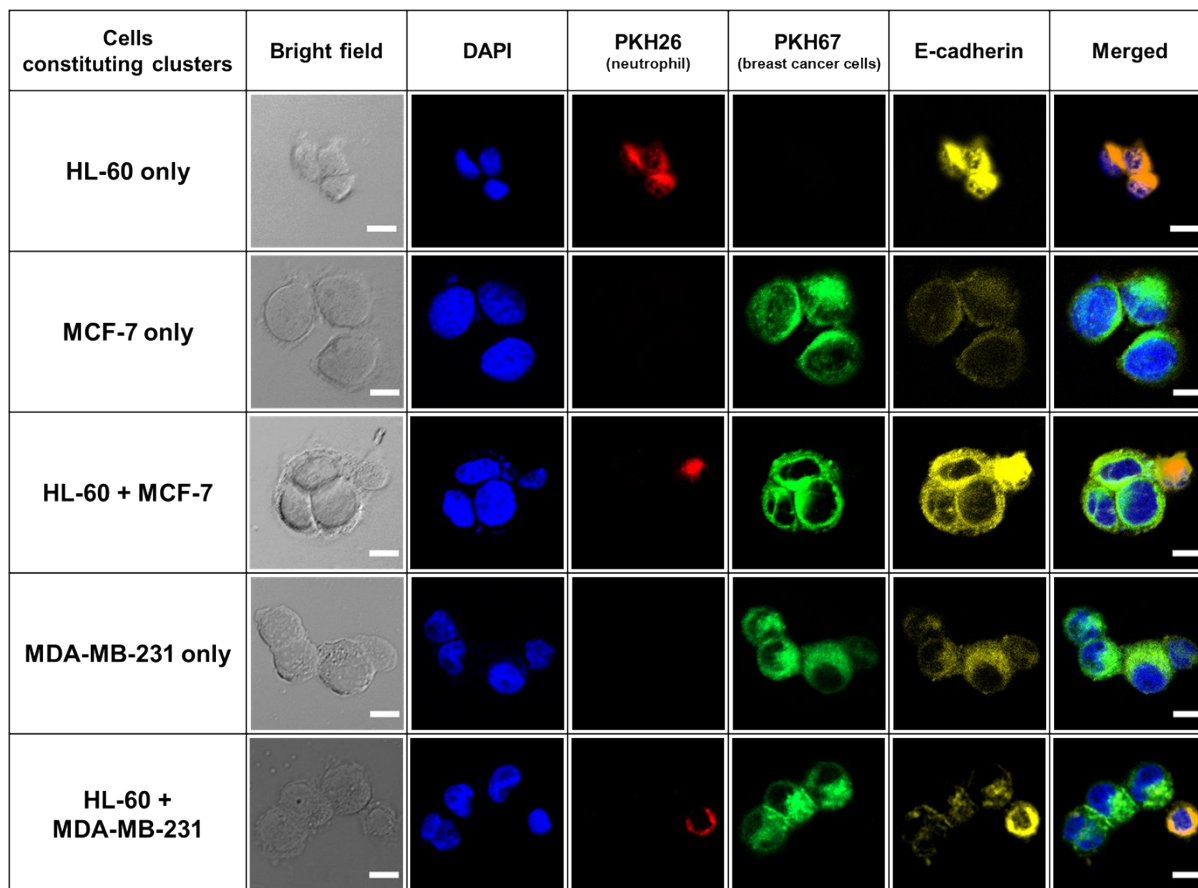


Fig. S4. Multi-fluorescence confocal microscopic images of five different combinations of clusters. The scale bars represent 10 μm .

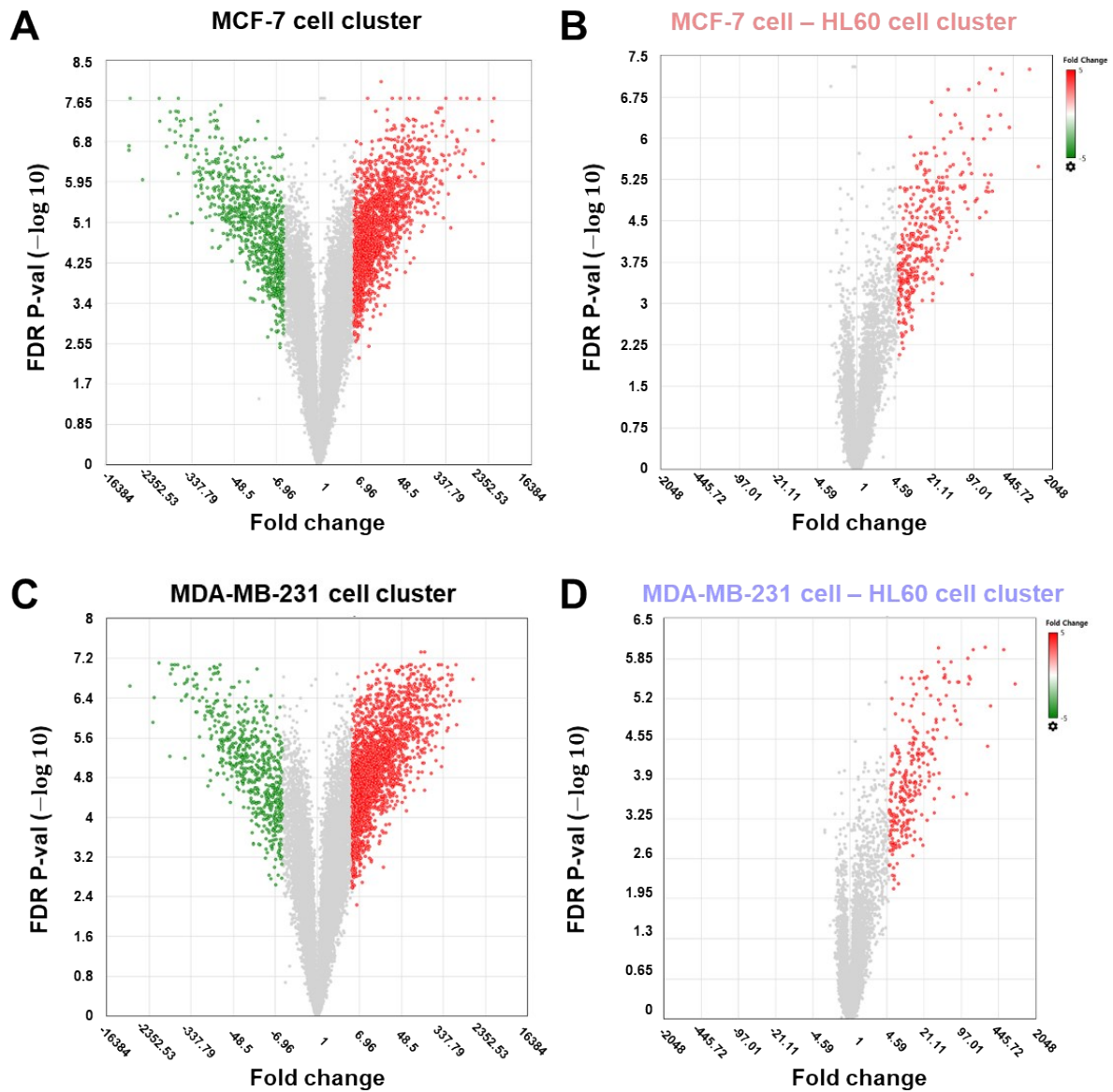


Fig. S5. Volcano plots summarizing the differentially expressed gene (DEG) analysis of neutrophil clusters, cancer-cell clusters, and cancer-cell–neutrophil clusters generated from the double-spiral chip. (A) Volcano plot showing DEGs in the MCF-7-cell (low-metastatic breast cancer cell line) cluster compared to the HL-60-cell cluster, indicating 465 down-regulated genes (green) and 1744 up-regulated genes (red). (B) Volcano plot showing the DEGs of the paired MCF-7-cell and HL-60-cell clusters, indicating 368 up-regulated genes (red) with respect to the MCF-7-cell cluster. (C) Volcano plot showing the DEGs of the MDA-MB-231-cell (high-metastatic breast cancer cell line) cluster compared with the HL-60-cell clusters,

indicating 215 down-regulated genes (green) and 1981 up-regulated genes (red). (D) Volcano plot showing the DEGs of the paired MCF-7-cell and HL-60-cell clusters, indicating 276 up-regulated genes (red) with respect to the MDA-MB-231-cell cluster.

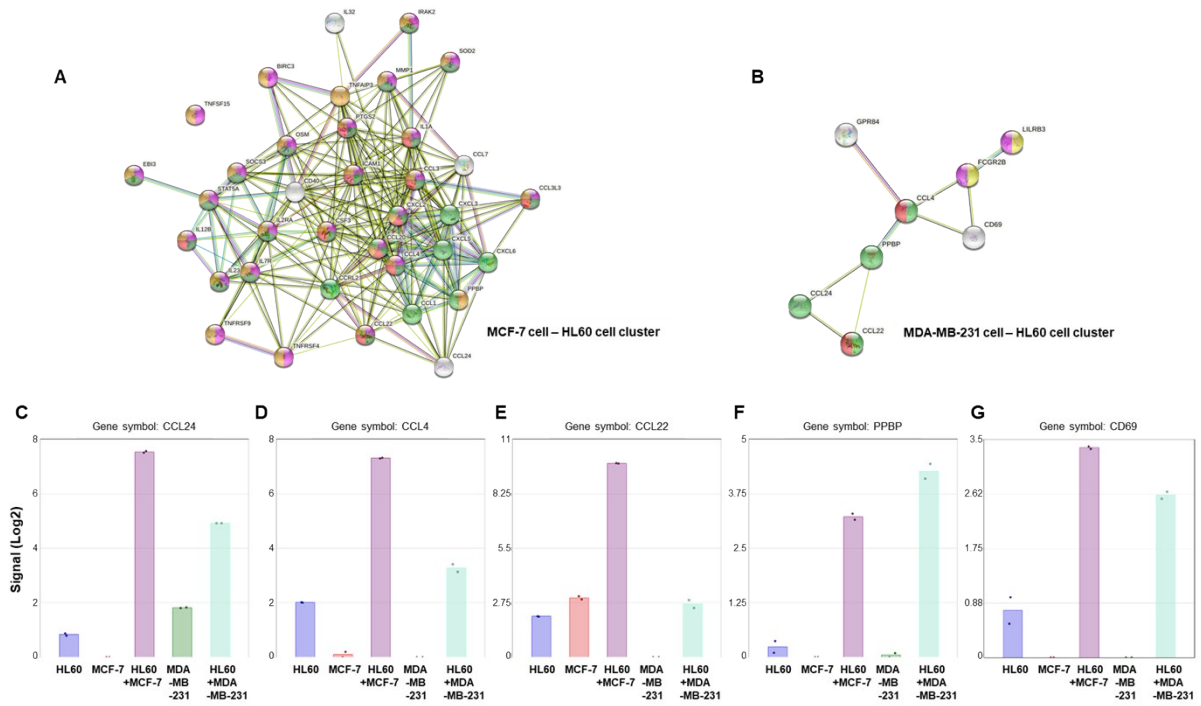


Fig. S6. Protein–protein interaction (PPI) network analysis of differentially expressed genes from (A) the clusters of MCF-7 cells with HL-60 cells and from (B) the clusters of MDA-MB-231 cells with HL-60 cells. The expression levels of (C) CCL24, (D) CCL4, (E) CCL22, (F) PPBP, and (G) CD69 were quantified by quantitative reverse transcription polymerase chain reaction (RT-qPCR) and exhibit significant over-expression in the clusters of both cancer cells and the HL-60 cells.

Table S1. Dimensionless numbers in the spiral channel with respect to flow rates.

Dimensionless number \ Flow rate (µl/min)	20	30	40	50	60	70
Channel Reynolds number	3.50	5.25	7.00	8.75	10.49	12.24
Particle Reynolds number, 12 µm bead	0.09	0.14	0.19	0.23	0.28	0.33
Particle Reynolds number, 15 µm bead	0.15	0.22	0.29	0.36	0.44	0.51
Dean number	0.36	0.54	0.72	0.90	1.07	1.25

Table S2. Functions of the key transcripts

	Gene	Function
CCL24	Chemokine (C-C motif) ligand 24	Metastasis, invasion
CCL4	Chemokine (C-C motif) ligand 4	Metastasis, invasion, TAM (tumor associated macrophages) recruitment
CCL22	Chemokine (C-C motif) ligand 22	Metastasis, invasion, immune-cell homeostasis
PPBP	Pro-platelet basic protein, CXCL7	Metastasis, pro-inflammation
CD69	Cluster of differentiation 69	Immune system, T-cell differentiation

References

- [1] A. S. Utada, A. Fernandez-Nieves, H. A. Stone and D. A. Weitz, *PRL*, 2007, **99**, 094502.
- [2] K. W. Oh, K. Lee, B. Ahn and E. P. Furlani, *Lab Chip*, 2012, **12**, 515-545.
- [3] A. J. T. Teo, K. H. H. Li, N. T. Nguyen, W. Guo, N. Heere, H. D, Xi, C. W. Tsao, W. Li and S. H. Tan, *Anal. Chem.*, 2017, **89**, 4387-4391.